

Calculation of x-ray spectra emerging from an x-ray tube;

Part I: Electron penetration characteristics in x-ray targets

Gavin G. Poludniowski^{a)} and Philip M. Evans

Joint Department of Physics, Institute of Cancer Research and The Royal Marsden NHS

5 *Foundation Trust, Downs Road, Sutton, Surrey SM2 5PT, United Kingdom*

The penetration characteristics of electron beams into x-ray targets are investigated for incident electron kinetic energies in the range 50 to 150 keV. The frequency densities of electrons penetrating to a depth x in a target, with a
10 fraction of initial kinetic energy, u , are calculated using Monte Carlo methods for beam energies of 50, 80, 100, 120 and 150 keV in a tungsten target. The frequency densities for 100 keV electrons in Al, Mo and Re targets are also calculated. A mixture of simple modelling with equations and interpolation from data is used to generalize the calculations in tungsten. Where possible,
15 parameters derived from the Monte Carlo data are compared to experimental measurements. Previous electron transport approximations in the semi-empirical models of other authors are discussed and related to this work. In particular the crudity of the use of the Thomson-Whiddington law to describe electron penetration and energy loss is highlighted. The results presented here
20 may be used towards calculating the target self-attenuation correction for bremsstrahlung photons emitted within a tungsten target.

I. INTRODUCTION

The accurate prediction of the photon spectrum emerging from an x-ray tube is important in imaging and therapy contexts, as the spectrum affects imaging properties
25 and patient dose. An understanding of the penetration characteristics of beams of

electrons into thick x-ray targets is necessary, as the depth of the associated x-ray production affects this spectrum via target self-filtration.

Determinations of the properties of electron transmission, using metal films, were
30 made by Whiddington¹ in 1912. That author found, empirically, that the square of the most probable energy of an electron, emerging from a film of thickness x , is approximately linearly dependent on x . The energy spectra of electron beams transmitted through slabs of media were investigated by later workers.²⁻⁴ A formula of the same form as for the most probable energy was shown to describe the mean
35 energy, $\langle T \rangle$, very well.⁴ This is referred to in the literature as the Thomson-Whiddington law and may be written:

$$\langle T(x) \rangle^2 = T_0^2 - C\rho x, \quad (1)$$

where T_0 is the kinetic energy of the incident electrons, ρ is target density and C is known as a Thomson-Whiddington constant. This last “constant” is approximately
40 material independent, but increases slowly with T_0 . Semi-empirical models of x-ray production have been proposed that make use of such a Thomson-Whiddington law to relate an electron’s energy to its penetration depth as a simple one-to-one mapping.⁵⁻¹⁰ Some of these models,⁷⁻⁹ amongst other approaches,¹¹ have been applied in a healthcare setting.¹² The values for the Thomson-Whiddington constants used in these
45 latter cases were those calculated by Birch and Marshall,⁷ using the extrapolated transmission range data of Katz and Penfold.¹³ The distribution in the energies of electrons at depth was ignored and backscatter was neglected.

This work addresses these issues using Monte Carlo electron transport. Whilst the
50 penetration characteristics of electrons have been investigated previously using Monte

Carlo methods e.g. Bishop¹⁴ or Sundararaman *et al.*,¹⁵ more recent articles have treated the entire process of x-ray generation, including the bremsstrahlung emission, using Monte Carlo e.g. Verhaegen *et al.*¹⁶ or Ay *et al.*¹⁷ With modern computing power and the careful use of variance reduction techniques, the full Monte Carlo simulation of an x-ray unit may, perhaps, be performed in a matter of minutes or less.¹⁸ However, the separation of the process of bremsstrahlung generation into two steps, electron penetration into a target and bremsstrahlung emission, can provide insight into the nature of beam transport in an x-ray target and the affect that this has on an emerging spectra. Examinations of the sufficiency of theoretical results for the differential bremsstrahlung cross-section are also readily made. This article, Part I, is the first of two papers. Here, the transport of electron beams corresponding to tube potentials of 50 to 150 kVp are simulated in an x-ray target using Monte Carlo methods. A second paper, Part II,¹⁹ presents spectral predictions using these results and bremsstrahlung cross-sections.

65

The primary objective of this paper, Part I, is to introduce, calculate and parameterize the “joint frequency density” describing electron penetration. This quantity, $f(u, x)$, is the number density of electrons that reach a depth x , with a fraction of the incident kinetic energy, u . This joint frequency density may be decomposed into a planar survival frequency, $\eta_{pl}(x)$, which is the frequency with which electrons reach a depth x , and the probability, $P(u/x)$, that an electron at that depth possesses an fraction of its initial energy, u . Then,

70

$$f(u, x) = \eta_{pl}(x)P(u | x). \quad (2)$$

The probability $P(u | x)$ will be referred to as the conditional probability function (CPF). Further, since an x-ray emission occurs within a thick target, it is convenient to

75

further decompose Eq. (2) into a first-pass (F) and a multiple-pass (M) component such that,

$$f(u, x) = \eta_F(x)P_F(u | x) + \eta_M(x)P_M(u | x). \quad (3)$$

The first-pass component corresponds to the quantity measured in transmission
 80 measurements, such as Whiddington's, through a slab of thickness x . The multiple-pass component is that one that is present due to backscatter from the material below the depth x . For the simple treatment developed here, it was necessary to demonstrate that a state of diffusion was reached rapidly in a target so that the angle of an electron at depth compared to its incident direction is independent of and uncorrelated to its
 85 kinetic energy.

II. THEORY AND METHOD

A. Scattering regions

Energetic electrons penetrating into thick high- Z materials undergo many scatters before coming to rest and several interaction processes are relevant.²⁰ The paths of the
 90 electrons are tortuous due to multiple deflections through elastic scattering. Consider electrons with the same initial kinetic energy incident normal to a target surface. Relatively infrequently an electron is kicked backwards in an interaction with the nucleus of an atom, a process which is sufficiently described by Rutherford or Mott scattering, but the majority of the scattering events are small angle deflections, in
 95 which the atomic cloud appreciably screens the nuclear potential. The first extremely thin layer of the target, corresponding to a few elastic mean free paths of penetration, is called the plural scattering region, and is normally assumed to apply where the number of scattering events is less than 20. This corresponds to $\sim 0.1 \mu\text{m}$ in tungsten for electrons with kinetic energies of tens of keV.²¹ By the time a few tens of mean
 100 free paths have been traversed, statistical averaging over an ensemble of electrons

results in a Gaussian angular distribution (for scattering angles less than $\sim 20^\circ$), with the most probable angle of an electron increasing with penetration depth. This is referred to as the multiple-scattering region. The final scattering region, diffusion, has been defined as the state in which the angular distribution of an electron beam
105 penetrating into a material no longer changes with depth.²⁰ In the elastic scattering of electrons from nuclei, energy loss is negligible, since the mass of a nucleus can be assumed infinite. In between elastic scattering events, however, inelastic scattering from electrons bound within the target atoms occurs, resulting in energy loss, ionisation, and knock-on electrons. The relative frequency of inelastic to elastic
110 scattering events is dependent on target atomic number and the electron energy, however, the elastic cross-section exceeds the inelastic for high- Z targets in the energy range of interest.

B. Geometry and angular distributions

The path of an electron in a target is depicted in Fig. 1. In this instance the primary
115 electron crosses a plane at a depth, x , three times before coming to rest. The path-length travelled at the n th crossing is denoted by l_n . The first crossing of the electron through the plane would be assigned, in an appropriate energy bin, as a “first-pass” and the second and third, in their appropriate energy bins, as “multiple-pass” contributions. The electron velocity at a depth x , is $\underline{V}(x)$. The incident electron
120 velocity vector, \underline{V}_0 , is aligned with the positive X-axis, normal to the surface of a semi-infinite target. The angle between these two vectors is the scattering angle, $\theta_s(l(x))$. Account must also be taken of knock-on electrons. δ -rays generated at a depth less than x , passing through x , may contribute to the first-pass component and δ -rays generated at a depth beyond x that are scattered backwards through the plane at
125 that depth are necessarily contributions to the multiple-pass component.

Within the target there will be a straggling in an electron's lateral displacement in the Y-Z plane, relative to its initial position, due to scatter. For a beam of a large enough area and sufficient intensity this may be neglected from the point of view of the origin of x-ray emissions. For every electron displaced from a Y-Z coordinate, there is one of the same kinetic energy to replace it at that location, excepting where an electron is close enough to the beam edge that its range may take it outside the original beam area. An electron beam used in general diagnostic x-ray tube has the approximate dimensions: $L \times L = 0.1 \times 0.1 \text{ cm}^2$.²² The typical penetration range for an electron in tungsten is $r \sim 10^{-3} \text{ cm}$. The fraction of electrons within range of edge-effects is therefore small, being: $4 \times L \times r / L^2 = 0.04$. It is therefore reasonable to treat electrons in a beam as if they had no lateral straggling from a macroscopic perspective i.e. from that of an ensemble of electrons emitting x-rays. Further, the beam spot-size increases little with depth and can be considered approximately the same as at the surface.

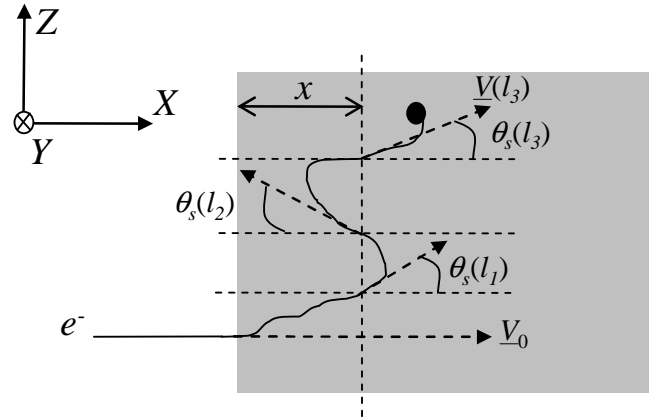


Fig. 1. Electron and target geometry and coordinate definitions.

Whilst an electron's lateral straggling may be ignored macroscopically, it is crucial to realise that its path-length, l , will be greater than the sum of its paths in the X-direction. That is, the average number of bremsstrahlung photons emitted per electron

per unit distance penetrated will be dependent on the angular distribution of the electron beam. This may be parameterized in a path-length correction. Azimuthal symmetry will be assumed in the angular distribution and the appropriate spherical
150 distribution must be projected onto a Y-Z plane. It is therefore convenient an angular distribution at diffusion, $h(\theta_s)$, with an associated normalisation,

$$\int_0^\pi d\theta_s h(\theta_s) = 1, \quad (4)$$

However, the sign of an electron's velocity vector with respect to the X-axis is immaterial to interaction probability and for certain purposes it is convenient to add
155 these contributions together to form a new distribution,

$$g(\theta_s) = h(\theta_s) + h(\pi - \theta_s), \quad (5)$$

where, now, $0 \leq \theta_s < \pi/2$. The diffusion angular distribution, in a scoring plane, for pure elastic scattering in an infinite medium is:²³

$$g_d(\theta) = 2 \cos \theta_s \sin \theta_s, \quad (6)$$

160 The factor $\sin \theta_s$ projects a spherical fluence distribution onto an annulus on the surface of a sphere and the factor $\cos \theta_s$ further projects onto the Y-Z plane.

Although an individual electron scatters many times between two planes separated by a distance of a fraction of a μm , if the beam is in diffusion, for each electron scattered
165 at a new angle, there is, on average, another electron of the same energy that scatters to replace it. The path-length correction then factorizes out into a multiplicative diversion factor. The mean diversion, d_x , will be defined,

$$d_x \equiv \left\langle \frac{\Delta l}{\Delta x} \right\rangle \xrightarrow{\text{diffusion}} \left\langle \frac{1}{\cos \theta_s} \right\rangle_{g(\theta_s)} = \int_0^{\pi/2} d\theta_s \frac{g(\theta_s, x)}{\cos \theta_s}. \quad (7)$$

This factor, assuming Eq. (6) is valid and that diffusion is reached instantaneously,
170 takes the value, $d_x = 2$.

C. Monte Carlo simulation

BEAMnrc²⁴ was used to simulate the penetration of normally incident monoenergetic electrons into a pure semi-infinite tungsten target using the EGSnrc Monte Carlo code.²⁵ Each simulation consisted of 4×10^6 electron histories and required
175 approximately one hour of CPU time. The Exact boundary crossing algorithm was used for electron transport and single-scattering was imposed by the choice of an appropriately large skin-depth (10^{10} mean-free-paths). The low incident electron kinetic energies of 50 to 150 keV made electron transport practicable without the condensation of multiple elastic scattering events into single steps. Spin-effects were
180 turned on. The values of AE and AP, determining the smallest energy-loss increment for stochastic treatment of inelastic collisions and bremsstrahlung, respectively, were set to 512 keV and 1 keV. The values of UE and UP, determining the high-energy cut-offs, for electrons and photons, respectively, were set to 1012 keV and 500 keV. In all simulations ECUT was set to 521 keV, such that each electron was transported until
185 its kinetic energy fell below 10 keV. As very few bremsstrahlung photons of energy less than 10 keV escape an x-ray unit, it was considered unnecessary to pursue electrons' progress beyond this cut-off. Phase-space files were generated at 0.5 or 1.0 μm increments of depths, with the maximum depth scored depending on the incident energy and varying between 2.5 μm and 14 μm . Five electron kinetic energies were
190 investigated: 50, 80, 100, 120 and 150 keV. Analysis of the phase-space files was performed using the BEAMDP analysis code.²⁶ The first-pass contributions to a phase-space file were analysed separately to the multiple-pass frequency, using "latching".²⁵ Simulations for aluminium, molybdenum, and rhenium were also

obtained, for $T_0 = 100$ keV only. These materials provide examples of low, medium
 195 and high-Z elements, respectively, to illustrate the affects of atomic number on the
 results. Molybdenum and rhenium are both commonly used materials in x-ray targets
 and many electron beam transmission measurements have used aluminium as their
 attenuating material.

D. First-pass frequency

200 Under diffusion conditions, the rate of decay of the first-pass frequency with
 penetration depth is expected to be proportional to the first-pass frequency itself:^{20,27}

$$d\eta_F = -\Sigma(x)\eta_F dx \quad (8)$$

where Σ is an attenuation coefficient related to the elastic and inelastic cross-sections.

A plausible form for η_F can be found heuristically without explicit knowledge of Σ .

205 In the non-relativistic limit, both the Mott cross-section describing elastic scatter and
 the Møller cross-section describing inelastic scatter, have an inverse square
 dependence on the kinetic energy of an electron. Hypothesizing an inverse square
 dependence for Σ :

$$\eta_F(x) \sim \exp\left(-\Sigma_0 \int_0^x \frac{T_0^2}{\langle T(x') \rangle_F^2} dx'\right) = \exp\left(-\Sigma_0 \int_0^x \frac{dx'}{\langle u(x') \rangle_F^2}\right). \quad (9)$$

210 where,

$$\langle u(x) \rangle_F = \langle T(x) \rangle_F / T_0 = \int_{\Lambda}^1 u P_F(u | x) du, \quad (10)$$

and where $\Lambda = 10$ keV/ T_0 and Σ_0 is an attenuation coefficient for electron with a
 kinetic energy, T_0 . If $\langle u(x) \rangle_F^2$ is replaced with the Thomson-Whiddington prediction,
 $u_{TW}(x)^2$, using Eq. (1), then after integration,

215
$$\eta_F = \left(u_{TW}^2\right)^\Gamma. \quad (11)$$

The constant $\Gamma \equiv \Sigma_0 R_{TW} / \rho$ is characteristic of the material and R_{TW} [mg·cm⁻²] is the Thomson-Whiddington range. This range is that as defined by the Thomson-Whiddington law: $R_{TW} = T_0^2 / C$, where C is the Thomson-Whiddington constant. This range should not be confused with the extrapolated range, R_{ex} [mg·cm⁻²], which is defined to be the value of intersection through the x-axis of a tangent to the η_F curve. These two quantities were equated in the work of Birch and Marshall⁷ and, hence, in the work dependent upon it.⁸⁻¹⁰ Care should be taken in equating these ranges with each other, as such identification will only be correct for a material in which the η_F curve is dominated by a linear portion.

225 **E. Multiple-pass frequency**

In a thick target, such as that in an x-ray tube, the backscatter from the deeper material must be accounted for at any given depth, ρx . The multiple-pass frequency, η_M , may be written as the sum of two contributions: the number of electrons moving forwards (η_+) and the number moving backwards (η_-). The forward and backward-moving numbers may be treated through the approximation of geometric series.^{28,29} Doing so,

$$\eta_- = \eta_F B (1 + (BF) + (BF)^2 + \dots) = \eta_F \frac{B}{1 - FB} \quad (12)$$

and

$$\eta_+ = \eta_- F, \quad (13)$$

where B and F are the backscatter and forward scatter fractions, respectively. B is the scatter back from the semi-infinite slab below the plane of interest and F is the forward scatter from the slab of finite thickness, x , above. The multiple-pass frequency is then,

$$\eta_M = \eta_+ + \eta_- = \eta_F B \left(\frac{F + 1}{1 - FB} \right) \quad (14)$$

and the planar survival frequency is, $\eta_{pl} = \eta_F + \eta_M = \eta_F + \eta_+ + \eta_-$. A related quantity
 240 is the planar survival current, $\eta_c = \eta_F + \eta_+ - \eta_-$. Whilst the survival current is
 constrained to satisfy $\eta_c \leq 1$, the survival frequency has no such constraint and, for
 this reason, it is to be interpreted as a frequency and not a survival probability.

At the target surface, necessarily,

245
$$F(\rho x) \Big|_{\rho x=0} = 0,$$

and at sufficient depth,

$$F(\rho x) \underset{\rho x \rightarrow \infty}{\sim} B(\rho x) \equiv B_d,$$

where B_d is the backscatter fraction at diffusion. The simplest parameterization for the
 forward-scatter between zero thickness and asymptotically large depths is therefore,

250
$$F(\rho x) = B_d \left(1 - \exp(-K \rho x / R_{TW}) \right), \quad (15)$$

where K is a dimensionless constant. This functional form exhibits an initial linear
 rise with ρx at small values of the exponent. This behaviour has been observed in
 backscatter experiments.²⁸

255 The angular distribution of the beam disperses from the incident δ -function towards
 the diffusion distribution as it penetrates and consequently, the backscatter factor
 initially increases with depth. Choosing the simplest parameterization to describe the
 transitory variation in the backscatter,

$$B(\rho x) = B_0 + (B_d - B_0) \left(1 - \exp(-K \rho x / R_{TW}) \right), \quad (16)$$

260 where B_0 is the backscatter fraction at the surface.

F. Conditional probability functions

Theoretical quantities related to the CPFs, $P_F(u/x)$ and $P_M(u/x)$, exist, such as Landau's and Vavilov's straggling functions.^{30,31,32} These straggling functions are defined in a non-trivial form, however, and furthermore, the functions are defined in terms of path-length rather than penetration depth. An empirical approach to describing the CPFs is preferred here. The first and multiple-pass components are treated separately, since the first-pass distribution is more amenable to experimental measurement, as it corresponds to the energy distribution of a beam exiting a slab of material, and some comparison to experimental findings can be made. The energy spectra for all depths and incident energies, for both the first-pass and multiple components, were generated from the Monte Carlo data in 2 keV bins over the ranges $10 < T < T_0$ keV. The CPFs were obtained by normalising the integral of these spectra over u to unity. A function was written in Matlab (MathWorks Inc., Natwick, MA) to linearly interpolate between the data sets in the u and x dimensions. For extrapolation of a CPF to an arbitrary initial kinetic energy, \hat{T}_0 , away from the values calculated, the following simple scaling rule is suggested:

$$P_i(u | x; \hat{T}_0) = P_i(u | xf; T_0) \quad (17)$$

where $i \in \{F, M\}$ and

$$f = R_{TW}(T_0) / R_{TW}(\hat{T}_0). \quad (18)$$

An approximate scaling in energy distributions has been identified elsewhere.²⁷

III. RESULTS

A. Validation of assumptions

Monte Carlo angular distributions for a 100 keV beam are presented in Fig. 2(a) at four depths. By a density-scaled depth of $2 \text{ mg}\cdot\text{cm}^{-2}$, equivalent to approximately 1 μm in tungsten, the distribution has converged. Fig. 2(b) shows the planar survival

frequency for those 100 keV electrons: it has decreased little at a depth of 2 mg cm⁻². Diffusion dominates then for the majority of the survival-frequency curve. Therefore, an electron beam of energy ~ 100 keV, incident upon a high-Z anode, reaches diffusion early in its journey into the target.

290

Fig. 3 presents the Monte Carlo results for the diffusion angular distributions of 50, 80, 100, 120 and 150 keV beams. The curves lie close together. The diffusion angular distribution is, to a good approximation, independent of incident electron energy in the range of interest. The close correspondence between the curves permits the use of the 100 keV angular distribution as a “universal distribution” for all the energies.

295

Fig. 4 shows the CPF, as defined by Eq. (2), for 100 keV incident electrons having penetrated to a depth of 3 μm (a density-scaled depth of 5.79 mg cm⁻²). The planar CPF was derived from the energy spectrum of planar electron fluence at depth, using BEAMDP analyses of Monte Carlo phase-space files. The path-corrected CPF, also shown, is defined by,

300

$$P_{Cor}(u | x) = \frac{1}{d_{DP}} P(u | x) \times \overline{(1/\cos \theta_s)}(u) \quad (19)$$

where

$$d_{DP} = \int_{\Lambda}^1 (P(u | x) \times \overline{(1/\cos \theta_s)}(u)) du \quad (20)$$

305 and $\overline{(1/\cos \theta_s)}(u)$ is the mean of the reciprocal of the cosine of the scattering angle, for electrons with an energy fraction, u . This second CPF was calculated from the “real fluence” as defined in the BEAMDP Users’ Manual.²⁶ The value of d_{DP} was found to be 1.88 for the example shown. The similarity in the shape of the two curves suggests

that the scattering angle of an electron at depth, is, to an excellent approximation,
 310 independent of the energy loss of a particle. This is in agreement with the sparse
 experimental literature available.²⁰

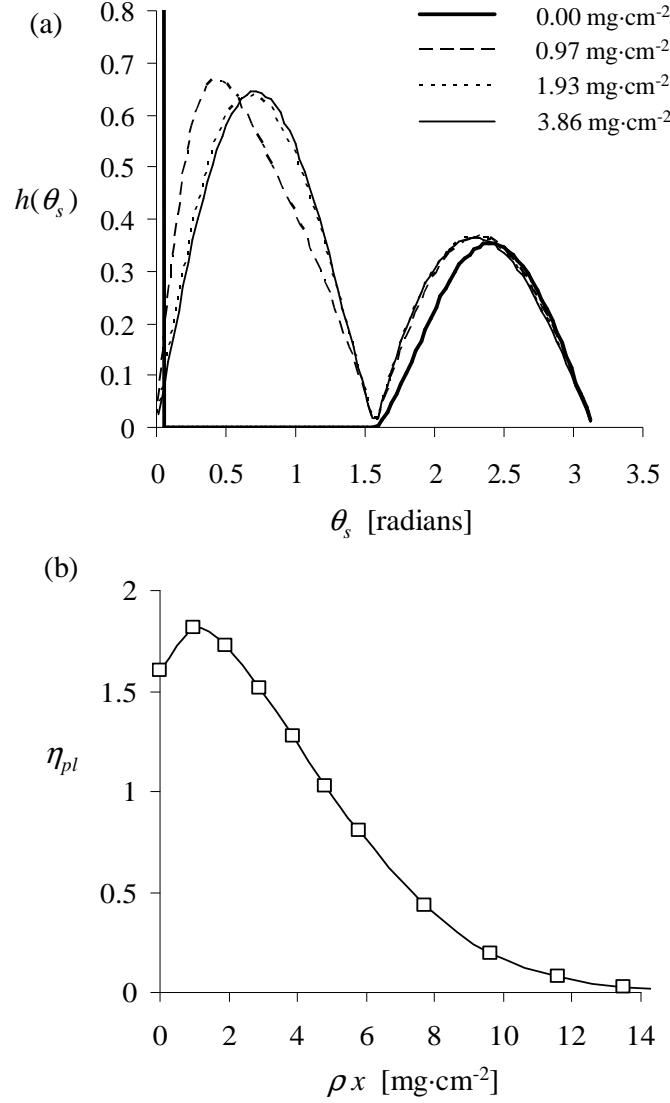
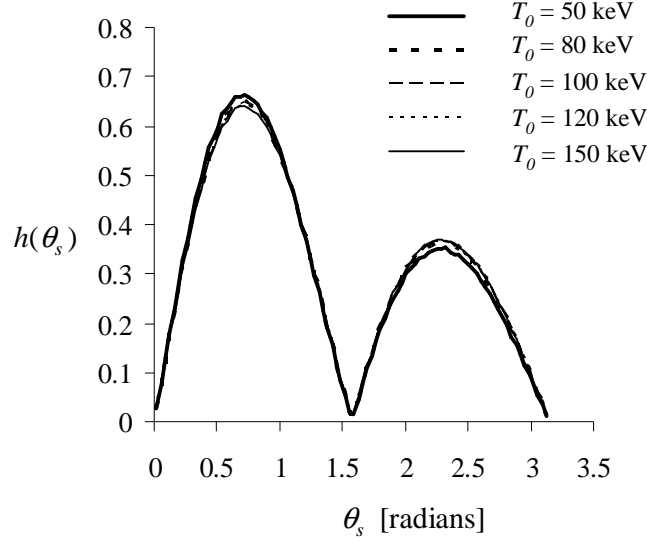
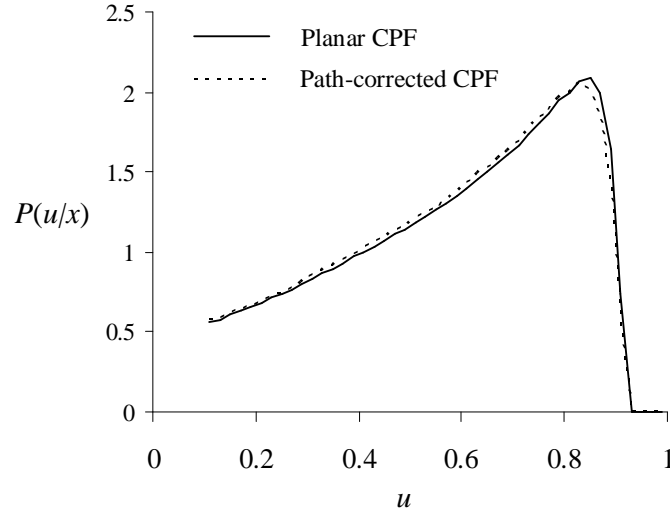


Fig. 2. For 100 keV incident electrons in tungsten, the (a) distribution of scattering angle at four depths and (b) planar survival frequency of the electrons (Monte carlo data).



315

Fig. 3. Diffusion angular distributions of scattering angles for electrons with incident kinetic energies of 50, 80, 100, 120 and 150 keV (Monte Carlo Data).



320 Fig. 4. Planar conditional probability function (solid line) and path-length corrected probability function (broken line), for electrons with an incident kinetic energy of 100 keV, at a density-scaled depth of 5.79 mg cm⁻² (Monte Carlo data).

B. Angular distribution

Fig. 5 displays the angular distribution $g(\theta_s)$, generated by Monte Carlo simulation in 2° bins, and the theoretical curve using Eq. (6). The agreement is good and hence

325 $d_x = 2.00$ is a reasonable approximation for the mean diversion. This is slightly

larger than, the value of 1.88 (d_{DP}) arrived at by another method in the previous subsection. This discrepancy is partly due to the fact that BEAMDP limits the obliquity with respect to the plane to less than 85° in calculating the “real fluence”. This cut-off is present to avoid large statistical fluctuations, due to the fact that the number of particles crossing a plane is asymptotically zero as $\theta_s \rightarrow \pi/2$. However, particle diversions approach infinity asymptotically in this limit, accentuating this contribution to the diversion factor such that it may not be completely negligible. To compare diversion estimates fairly, Eq. (7) should be modified to give

$$d_{85^\circ} = \int_{0^\circ}^{85^\circ} \frac{g(\theta_s)}{\cos \theta_s} d\theta_s + \frac{1}{\cos 85^\circ} \int_{85^\circ}^{90^\circ} g(\theta_s) d\theta_s = 1.91, \quad (21)$$

where again Eq. (6) has been assumed for the diffusion distribution. The remaining small discrepancy is due to the imperfect nature of the fit of Eq. (6) to the angular distribution data. Henceforth it will be assumed that: $d_x = 2.00$.

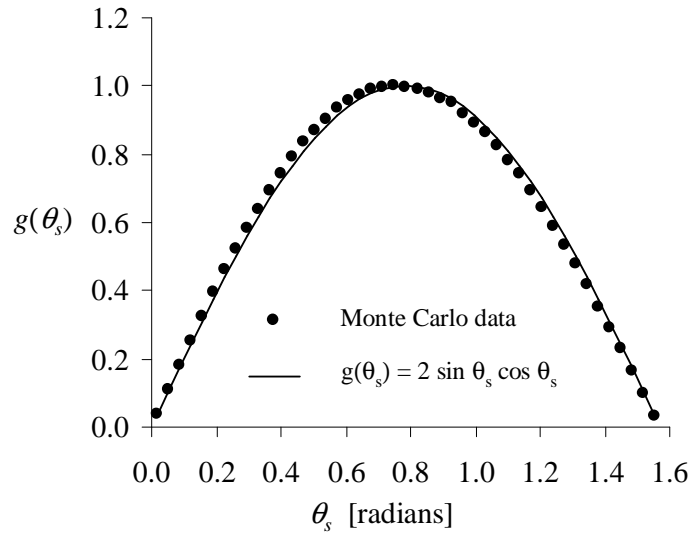


Fig. 5. Angular distribution, $g(\theta_s)$, for a 100 keV incident electron energy, at a density-scaled depth of 5.79 mg cm^{-2} (Monte Carlo data). The predictions of Eq. (6) also shown (solid curve).

C. Thomson-Whiddington law and the mean energy

The square of the mean energy of a beam emerging from a target layer will approach zero asymptotically as the thickness of the slab approaches infinity. The use of the Thomson-Whiddington law to describe this quantity is based upon fitting a straight-
 345 line to the initial, approximately linear, part of the curve. The data points in Fig. 6(a) show the Monte Carlo results for $\langle u \rangle_F$ at five different incident energies. The solid curves were generated using the fit

$$\langle u \rangle_F^2 = b \cdot (\rho x)^2 - c \cdot (\rho x) + 1.00, \quad (22)$$

where $b = 5999 \cdot T_0^{-3.148} \text{ [mg}^{-2} \cdot \text{cm}^4]$ and $c = 130.1 \cdot T_0^{-1.559} \text{ [mg}^{-1} \cdot \text{cm}^2]$. The two-
 350 dimensional correlation coefficient for the fit was $R^2 = 0.997$. The broken curves in the figure correspond to linear fits (fitting for $\langle u \rangle_F^2 > 0.4$). The corresponding Thomson-Whiddington constants (C) are presented in Table 1, along with the values presented by Birch and Marshall⁷ (C_{BM}). The linear relation is good in the region of fitting. There is, however, a failure to describe the onset of the asymptotic regime
 355 apparent in the data ($\langle u \rangle_F^2 < 0.4$). The Thomson-Whiddington range, as defined by C , is well-described ($R^2 = 0.999$) by,

$$R_{TW} = 0.0119 \cdot T_0^{1.513} \text{ [mg} \cdot \text{cm}^{-2}]. \quad (23)$$

The exponent of T_0 is very close to the energy-dependence of the extrapolated ranges of Katz and Penfold.¹³ Their predictions were 1.446 at $T_0 = 150 \text{ keV}$ and 1.551 at $T_0 =$
 360 50 keV .

The fall of $\langle u \rangle_F^2$ with penetration depth for aluminium, molybdenum, rhenium and tungsten are presented in Fig. 6(b). The rate of fall is only weakly dependent on the atomic number of the target material. The fall of $\langle u \rangle_M^2$ for aluminium, molybdenum,

365 rhenium and tungsten are presented in Fig. 7(b). There is a more sizable variation
between materials, with aluminium showing the largest discrepancy with respect to
the tungsten results. The fall of $\langle u \rangle_M^2$ with depth in tungsten, in the range
 $50 < T_0 < 150$ keV, displayed in Fig. 7(a), is well described ($R^2 = 0.996$ in two
dimensions) by,

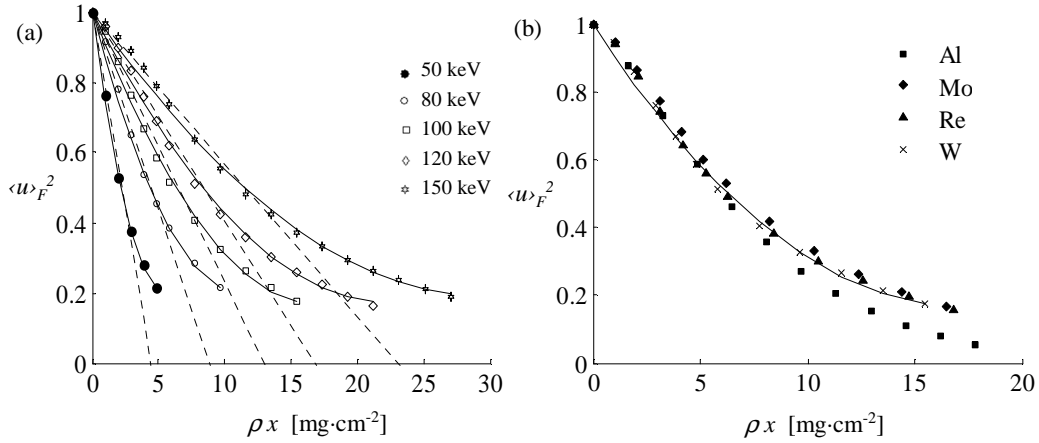
370
$$\langle u \rangle_M^2 = -a \cdot (\rho x)^3 + b \cdot (\rho x)^2 - c \cdot (\rho x) + 0.61 \quad (24)$$

where $a = 15859 \cdot T_0^{-3.903} [\text{mg}^{-3} \cdot \text{cm}^6]$, $b = 1016 \cdot T_0^{-2.544} [\text{mg}^{-2} \cdot \text{cm}^4]$ and

$c = 32.5 \cdot T_0^{-1.249} [\text{mg}^{-1} \cdot \text{cm}^2]$.

T_0 [keV]	C [$\text{keV}^2 \cdot \text{mg}^{-1} \cdot \text{cm}^2$]	C_{BM} [$\text{keV}^2 \cdot \text{mg}^{-1} \cdot \text{cm}^2$]
50	565	540
80	710	639
100	792	700
120	865	787
150	964	840

Table 1. Thomson-Whiddington constants derived from the Monte Carlo data and the corresponding R^2 -correlation. The Birch and Marshall values for Thomson-Whiddington constants are also quoted.⁷



375

Fig. 6. $\langle u \rangle_F$ as a function of penetration for (a) five initial electron energies and for (b) aluminium, molybdenum, rhenium and tungsten at a 100 keV incident energy (Monte Carlo data). The solid curves are polynomial fits using Eq. (22) and the dotted lines are the Thomson-Whiddington predictions the values of C appearing in Table 1.

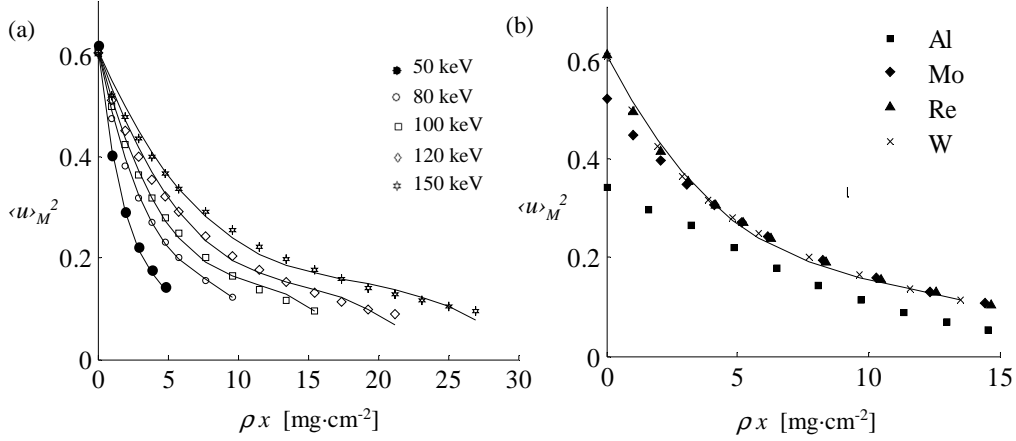


Fig. 7. $\langle u \rangle_M^2$ as a function of penetration for (a) five initial electron energies and for (b) aluminium, molybdenum, rhenium and tungsten at a 100 keV incident energy (Monte Carlo data). The solid curves are polynomial fits using Eq. (24).

D. First and multiple-pass frequencies

The first and multiple-pass frequencies for 100 keV incident electrons are shown in Fig. 8(a) and Fig. 8(b) for tungsten, rhenium, molybdenum and aluminium. The tungsten ($Z = 74$ and $\rho = 19.3 \text{ mg}\cdot\text{cm}^{-3}$) and rhenium ($Z = 75$ and $\rho = 21.0 \text{ mg}\cdot\text{cm}^{-3}$) results are essentially identical, as expected for two elements differing by only one unit in atomic number and having very similar densities. Molybdenum ($Z = 42$ and $\rho = 10.3 \text{ mg}\cdot\text{cm}^{-3}$) shows a marked departure from tungsten. Aluminium ($Z = 13$ and $\rho = 2.7 \text{ mg}\cdot\text{cm}^{-3}$) shows a considerable difference. The shape of the curve is sensitive to Z . The plural scattering, multiple-scattering and diffusion regions have been identified with an inflection, a linear portion and an exponential fall in η_F , respectively.²⁰ The extent of the plural and multiple-scattering regions is expected to diminish with increasing Z and this is confirmed by the graphs. Tungsten is dominated by an exponential-looking rate of fall, molybdenum has a fairly large linear portion and aluminium exhibits a definite initial inflection. The lack of a clear linear portion in high- Z targets means that an extrapolated range (R_{ex}) cannot be unambiguously defined. For aluminium, a low- Z target, an extrapolated

range can be found unambiguously. The solid line on Fig. 8(a) shows a fit to the linear
 portion: the extrapolated range was $12.7 \text{ mg}\cdot\text{cm}^{-2}$. Katz and Penfold presented
 Carlvik's experimental value of $13.0 \pm 0.5 \text{ mg}\cdot\text{cm}^{-2}$ for this range, consistent with the
 value derived here. Further, using a continuous-slowing-down approximation (CDSA)
 range of $18.7 \text{ mg}\cdot\text{cm}^{-2}$ for 100 keV electrons incident on aluminium, the method of
 Tabata *et al.*³³ predicts an extrapolated range of $12.4 \text{ mg}\cdot\text{cm}^{-2}$, also close to the value
 found in this work.

The first and multiple-pass frequencies are presented in Fig. 9(a) and Fig. 9(b) for
 tungsten and electron energies of 50, 80, 100, 120 and 150 keV. The solid curves are
 the best-fits making use of Eqs. (11) and (14) to (16). The data are suitably described
 by the forms of these equations with the parameter Γ held constant, independent of T_0 .
 The values of the constants found, for tungsten, were $\Gamma = 1.753$, $K = 18.0$ and $B_d =$
 0.584 . The value of the surface backscatter, B_0 , was calculated from $B_0 \equiv \eta_M(x=0)$
 and found to take the value 0.50.

The values of parameters quoted were determined from the data for the first-pass (η_F)
 and multiple-pass frequencies ($\eta_M = \eta_+ + \eta_-$). The solid squares in Fig. 10 depict η_-
 and the empty squares η_+ , for 100 keV electrons incident on tungsten. The curves
 through these points are the fit using Eq. (12) and Eq. (13) and the parameter values
 quoted above. The fit is good, despite these parameters having been determined from
 the sum of η_- and η_+ , not their independent values. This therefore validates the use
 of the geometric series approach. Both η_+ and η_- are modelled correctly.

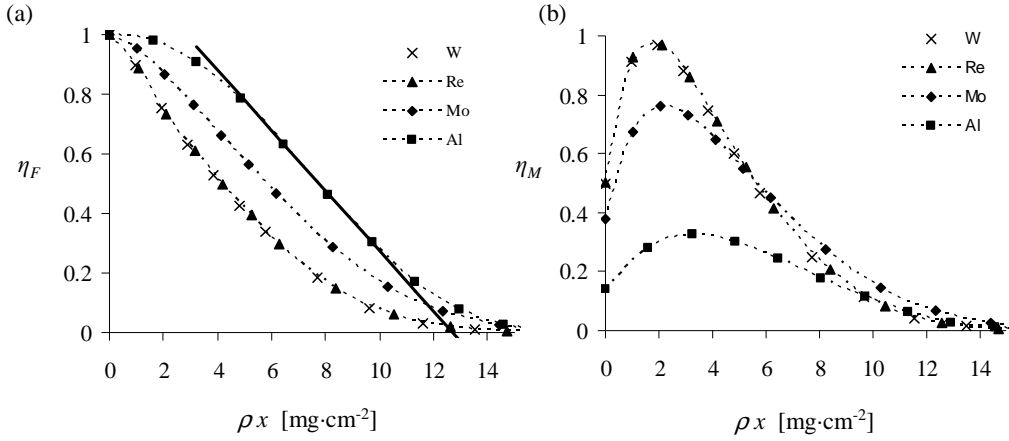


Fig. 8. The (a) first-pass frequencies and (b) multiple-pass frequencies, for 100 keV electrons

425 penetrating into four different elements (Monte Carlo data).

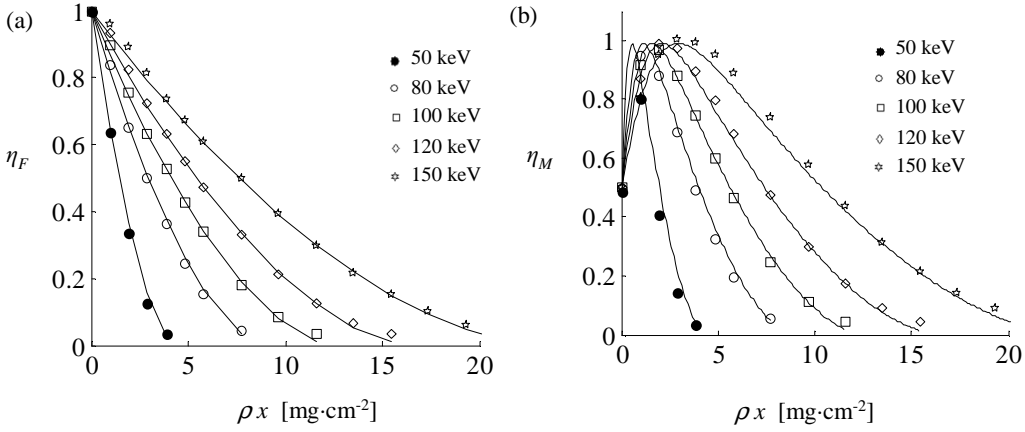
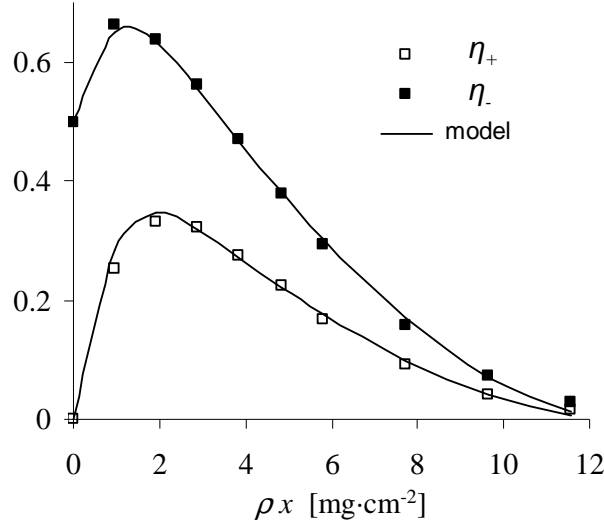


Fig. 9. The (a) first-pass frequencies and (b) multiple-pass frequencies for electrons penetrating into tungsten with five different incident energies (Monte Carlo data). Solid curves are best-fits using Eqs. (11) and (14) to (16).



430 Fig. 10. The values of the η_+ and η_- frequencies for 100 keV electrons incident on tungsten (Monte Carlo data). Solid lines are the predictions using Eq. (12) and (13) and the values of constants quoted in the text.

E. Energy distribution

435 The shape of the CPF functions of 100 keV incident electrons at density-scaled depths of 1.93, 5.79 and 11.58 mg·cm⁻² are presented in Fig. 11. The data points (circles) correspond to the Monte Carlo results binned in 2 keV increments. The solid curves are linear interpolations in u and x . Unsurprisingly, the multiple-pass CPFs are broader than their first-pass counterparts and exhibit lower mean values of u . Note, however, that the first-pass component becomes rapidly more broad as it penetrates. Also, note the long low energy tail, present partly due to the generation of δ -rays,³⁴ the so-called Landau tail, but also arising from the distribution of path lengths of electrons at a given depth. The maximum cut-off in u is absolute (rather than asymptotic) and is present due to the CSDA component of energy loss in EGSnrc.

445 This cut-off decreases linearly with depth.

The CPF functions at a density-scaled depth of 3.86 mg·cm⁻² are presented in Fig. 12 for five incident electron energies. Not only are less energetic electrons less

penetrative, they also, as these results demonstrate, exhibit a broader distribution in
 450 energies at the same depth. This is despite possessing an essential identical angular
 distribution. The broken curves are linear interpolations of the Monte Carlo data at the
 relevant incident energy. The solid curves are the predictions using Eq. (17) and Eq.
 (18) with Monte Carlo data for $T_0 = 100$ keV, and linear interpolation in x and u . The
 scaling law for extrapolation to arbitrary energy performs well.

455

Example data (circles) of the CPFs of rhenium, molybdenum and aluminium are
 presented in Fig. 13, at similar values of density-scaled depth. The solid curves are
 the predictions using linear interpolation in u and x , between tungsten data. The CPF
 of rhenium is seen to very closely match the interpolation prediction in tungsten.
 460 Molybdenum shows a discernable discrepancy with the prediction based on tungsten
 and in aluminium the agreement is poor. This is unsurprising, as the ratio of elastic to
 inelastic scatter varies markedly as Z decreases³⁵ and the different balance of
 scattering mechanism inevitably affects the character of energy loss with depth. The
 shift of the CPF curve for aluminium towards lower energies with respect to the
 465 tungsten curve is consistent with Cosslett and Thomas' experimental results for
 aluminium and gold, with incident electrons of 18 keV.⁴

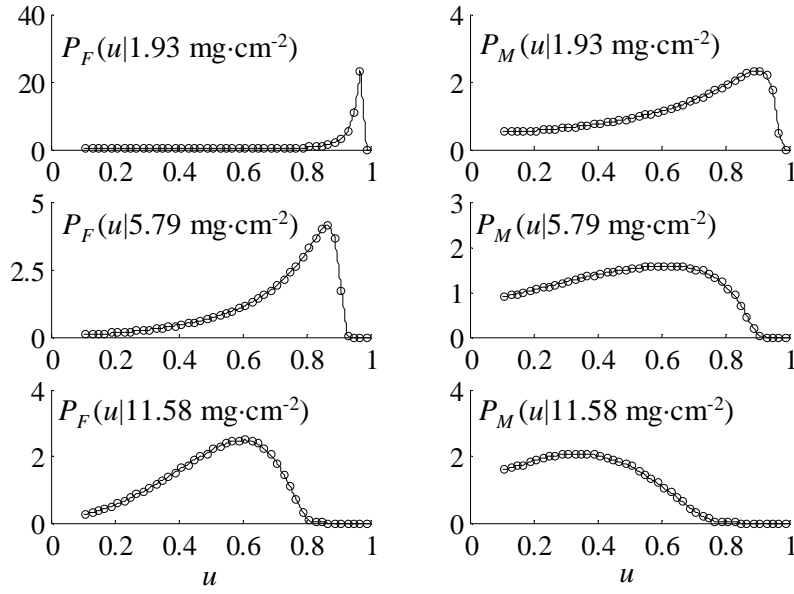


Fig. 11. The first-pass (P_F) and multiple pass (P_M) CPFs for electrons of initial kinetic energy 100 keV, at three depths in tungsten (Monte Carlo data). The solid curves are linear interpolations.

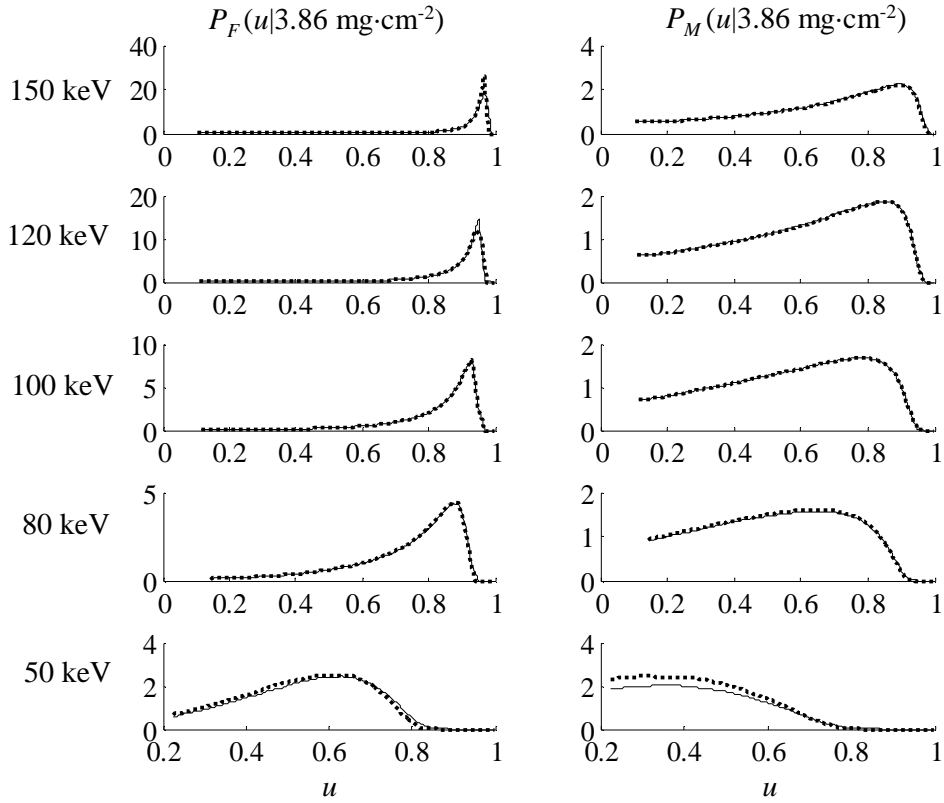


Fig. 12. The first-pass (P_F) and multiple-pass (P_M) CPFs for five different initial electron kinetic energies at a density-scaled depth of $3.86 \text{ mg}\cdot\text{cm}^{-2}$ in tungsten. The solid curves are linear

interpolations (in u) between Monte Carlo data of 100 keV incident electrons and extrapolation to other energies using Eqs. (17) and (18).

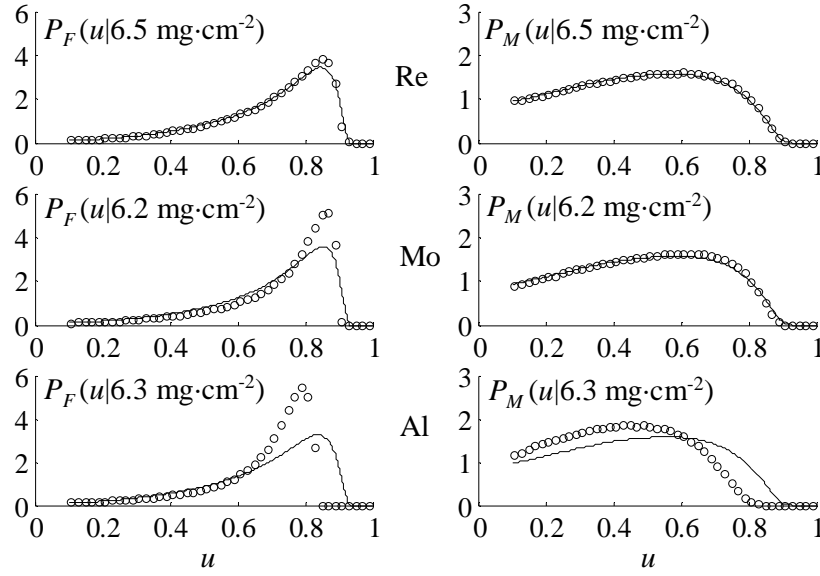


Fig. 13. The first-pass (P_F) and multiple-pass (P_M) CPFs for rhenium, molybdenum and aluminium at similar values of ρx (Monte Carlo data). The solid lines are the predictions for the stated density-scaled depth, based on interpolation in u and x between 100 keV electrons in tungsten data.

IV. DISCUSSION

The results of section III.A demonstrate that diffusion is reached rapidly, rapidly enough to assume, to a reasonable approximation, that it is instantaneous. The scattering angle of an electron was also shown to be sufficiently independent of its kinetic energy to factorise the θ -dependence from the u -dependence. These facts allow the calculation of a simple multiplicative path-length correction for high- Z materials, using Eq. (7), which is (approximately) valid for all incident energies of interest ($50 < T_0 < 150$ keV). This diversion correction, d_x , was found in section III.B to take an approximately constant value of 2.

The analysis presented in section III.C showed that the Thomson-Whiddington law

provided a good approximation for $\langle u(x) \rangle_F$ only when $\langle u \rangle_F^2 > 0.4$. Nevertheless,

since the first-pass survival frequency η_F declines more rapidly with depth than $\langle u \rangle_F$ (Section III.D), the Thomson-Whiddington law provides a fair approximation at the depths where η_F is appreciably large. The values of the Thomson-Whiddington constants presented in Table 1 correspond fairly closely with the value quoted by
 495 Birch and Marshall, which are used in several x-ray spectra models.⁷⁻¹⁰ It is unsurprising that their values are somewhat different to those of this work, as they were derived from the extrapolated range data summarised by Katz and Penfold¹³ based on low-Z materials, predominantly aluminium. Fig. 6 showed that there is some deviation of the aluminium data from the results of tungsten. In addition, whilst it is
 500 perhaps legitimate to identify the extrapolated range with the Thomson-Whiddington range for low-Z materials, care should be taken in doing so for high-Z materials like tungsten, for which, as Fig. 8 clearly shows, there is no discernable linear portion.

There remain several ways to model the joint frequency density and hence the
 505 penetration of electrons into a target. Four of these are, in increasing order of sophistication,

$$f(u, x) = \delta(u - u_{TW}(x)), \quad (25a)$$

$$f(u, x) = \eta_F(x) \delta(u - u_{TW}(x)), \quad (25b)$$

$$f(u, x) = \eta_F(x) \delta(u - \langle u(x) \rangle_F) + \eta_M(x) \delta(u - \langle u(x) \rangle_M), \quad (25c)$$

$$510 \quad f(u, x) = \eta_F(x) P_F(u | x) + \eta_M(x) P_M(u | x). \quad (25d)$$

Approach (25a) was, implicitly, that taken by Birch and Marshall⁷ and others.⁸⁻¹⁰ Whilst this approach has the virtue of simplicity, it ignores the distribution of electron energies at depth (a Dirac δ -function imposed), ignores backscatter (absence of a multiple-pass term) and, furthermore, ignores the possibility that an electron does not

515 survive to a given depth (absent η_F term). Approach (25b) remedies the last deficit.
Approach (25c), in addition, introduces backscatter. Finally, (25d) provides the full
description in terms of the model developed here. The degree of backscatter is not
small: that is η_M is not small compared to η_F (Section III.D). Monte Carlo results
therefore suggest that at the very least, approach (25c) should be adopted. Further, the
520 rapid broadening of both the first and multiple-pass CPFs demonstrated in section
III.E suggests that this third approach may not give a good approximation to the full
model. The formalism introduced in this work allows the full, most sophisticated
model, to be applied to the problem of electron beam penetration in a high-Z target.
The results presented here may be used towards calculating the spectra of
525 bremsstrahlung escaping an anode. This aim is pursued in the companion paper, Part
II.¹⁹

It is noteworthy that the results of this paper are derived from Monte Carlo modelling,
not experiment. It has been assumed here that the physical model contained in the
530 EGSnrc code, with the options that were selected, adequately encapsulates the
relevant physics in the electron kinetic energy range of 10 to 150 keV. The EGSnrc
code system has, however, excelled in validation exercises of its electron transport^{36,37}
and certain parameters derived in this work, such as R_{ex} for aluminum, have agreed
with experimental results. It seems likely, in any case, that the beam transport results
535 presented here are a great quantitative improvement on the methods hitherto used in
the models of x-ray spectra where the Thomson-Whiddington relation has been used.

The results presented here for the survival frequencies and CPFs should be applicable
for heavy elements of atomic numbers similar to tungsten. They may also be of some

540 applicability for elements of moderate- Z such as molybdenum. It should be noted that there are x-ray tubes in use within healthcare that possess anodes made of elements that are not high- Z materials. The majority of such tubes are used in mammography. The tube potentials used in these cases are less than 50 kVp, outside of the range investigated here. If the approach adopted here were to be repeated and applied to
545 mammographic energies and lower Z materials, careful consideration would have to be taken of the consequences of the less rapid onset of diffusion.

V. CONCLUSION

The concept of the joint frequency density, describing electron penetration in a target, was introduced and decomposed into survival frequencies and conditional probability
550 functions. These components were calculated using Monte Carlo techniques for electron beams of energies of 50, 80, 100, 120 and 150 keV penetrating into a thick tungsten target. Results for low and medium atomic number targets were compared for 100 keV beams. A combination of parameterization in the form of equations, interpolation in energy fraction and depth, and extrapolation in incident beam energy,
555 were used to generalise the results. The results of this paper allow the more accurate treatment of the penetration of electrons into high- Z targets, for use in models of x-ray spectra generation.

ACKNOWLEDGEMENTS

The authors would like to thank Laure Parent and David Roberts for their assistance
560 with aspects of the Monte Carlo work and both Mike Partridge and Emma Harris for their comments on an early draft of this paper. The authors would also like to thank the referees for their comments. This work was supported by Cancer Research UK Programme Grant C46/A3970.

^{a)}Electronic mail: Gavin.Poludniowski@icr.ac.uk

- ¹R. Whiddington, "The transmission of cathode rays through matter," Proc. R. Soc. London Ser. A **86**, 360-370 (1912).
- ²O. Klemperer, "Über Geschwindigkeitsverluste von Kathodenstrahlen in Metallfolien," Z. Phys. **34**, 532 (1925).
- 570 ³J. R. Young, "Dissipation of Energy by 2.5-10 keV Electrons in Al₂O₃," J. Appl. Phys. **28** (2), 524-525 (1957).
- ⁴V. E. Cosslett and R. N. Thomas, "Multiple scattering of 5-30 keV electrons in evaporated metal films II: Range-energy relations," Br. J. Appl. Phys. **15**, 1283-1300 (1964).
- 575 ⁵P. Tothill, "The ratio of K characteristic to total radiation emitted from a tungsten target x-ray tube," Br. J. Appl. Phys. **2** (1), 1093-1107 (1968).
- ⁶B. W. Soole, "The effect of target absorption on the attenuation characteristics of bremsstrahlung generated at constant medium potentials," J. Phys. B **5**, 1583-1595 (1972).
- 580 ⁷R. Birch and M. Marshall, "Computation of Bremsstrahlung X-ray Spectra and Comparison with Spectra Measured with a Ge(Li) Detector," Phys. Med. Biol. **24** (3), 505-517 (1979).
- ⁸D. M. Tucker, G. T. Barnes and D. P. Chakraborty, "Semiempirical model for generating tungsten target x-ray spectra," Med. Phys. **18** (2), 211-218 (1990)
- 585 ⁹K. Cranley, B. J. Gilmore, G. W. A. Fogarty and L. Deponds, "Catalogue of diagnostic x-ray spectra and other data," IPEM Report 78 (The Institute of Physics and Engineering in Medicine, York, 1997).
- ¹⁰M. M. Blough, R. G. Waggener, W. H. Payne and J. A. Terry, "Calculated mammographic spectra confirmed with attenuation curves for molybdenum, rhodium, and tungsten targets," Med. Phys. **25** (9), 1605-1612 (1998).
- 590

- ¹¹J. H. Siewerdsen, A. M. Waese, D. J. Moseley, S. Richard and D. A. Jaffray, "Spektr: a computational tool for x-ray spectral analysis and imaging system optimization," *Med. Phys.* **31**, 3057-3067 (2004).
- ¹²P. Meyer, E. Buffard, L. Mertz, C. Kennel, A. Constantinesco and P. Siffert, "Evaluation of the use of six diagnostic X-ray spectra computer codes," *Br. J. Radiol.* **77**, 224-230 (2004).
- ¹³L. Katz and A. S. Penfold, "Range-Energy Relations for Electrons and the Determination of Beta-Ray End-Point Energies by Absorption," *Rev. Mod. Phys.* **24** (1), 28-44 (1952).
- ¹⁴H. E. Bishop, "Electron scattering in thick targets," *Br. J. Appl. Phys.* **18**, 703-715 (1967).
- ¹⁵V. Sundararaman, M. A. Prasad and R. B. Vora, "Computed Spectra from Diagnostic and Therapeutic X-ray Tubes," *Phys. Med. Biol.* **18** (2), 208-218 (1973).
- ¹⁶F. Verhaegen, A. E. Nahum, S. Van de Putte and Y. Namito, "Monte Carlo modelling of radiotherapy kV x-ray units," *Phys. Med. Biol.* **44**, 1767-1789 (1999).
- ¹⁷M. R. Ay, M. Shahriari, S. Sarkar, M. Adib and H. Zaidi, "Monte Carlo simulation of x-ray spectra in diagnostic radiology and mammography using MCNP4C," *Phys. Med. Biol.* **49**, 4897-4917 (2004).
- ¹⁸E. Mainegra-Hing and I. Kawrakow, "Efficient x-ray tube simulations," *Med. Phys.* **33** (8), 2683-2690 (2006).
- ¹⁹G. G. Poludniowski, "Calculation of x-ray spectra emerging from an x-ray tube; Part II: X-ray production and filtration in x-ray targets," *submitted to Med. Phys.*
- ²⁰V. E. Cosslett and R. N. Thomas, "Multiple scattering of 5-30 keV electrons in evaporated metal films I: Total transmission and angular distribution," *Br. J. Appl. Phys.* **15**, 883-907 (1964).

- ²¹V. E. Cosslett and R. N. Thomas, "The plural scattering of 20 keV electrons," Br. J. Appl. Phys. **15**, 235-248 (1964).
- ²²IPEMB, *Report 32: Measurement of the Performance Characteristics of Diagnostic X-ray Systems used in Medicine, Part I: X-ray Tubes and Generators* (IPEMB, York, 1995).
- ²³S. Goudsmit and J. L. Saunderson, "Multiple scattering of electrons," Phys. Rev **57**, 24-29 (1940)
- ²⁴D. W. O. Rogers, C.-M. Ma, G. X. Ding, B. Walters, D. Sheikh-Bagheri, and G. G. Zhang, *NRCC Report PIRS-0509(A)revK: BEAMnrc Users Manual* (NRCC, Ottawa, Canada, 2004).
- ²⁵I. Kawrakow and D. W. O. Rogers, *NRCC Report PIRS-701: The EGSnrc Code System* (NRCC, Ottawa Canada, 2003).
- ²⁶D.W.O. Rogers, C.M. Ma, G.X. Ding and B. Walters, National Research Council Report PIRS-0509(A): BEAMDP Users' Manual (NRCC, Ottawa, Canada, 1995).
- ²⁷H. J. Fitting, "Transmission, energy distribution, and SE excitation of fast electrons in thin solid films," Phys. Status Solidi **26**, 525-535 (1974).
- ²⁸V. E. Cosslett and R. N. Thomas, "Multiple scattering of 5-30 keV electrons in evaporated metal films III: Backscattering and absorption," Br. J. Appl. Phys. **16**, 779-796 (1965).
- ²⁹V. Lantto, "An empirical treatment of energy dissipation of fast electrons at normal incidence in semi-infinite targets," J. Phys. D **6**, 1058-1066 (1973).
- ³⁰L. D. Landau, "On the energy loss of fast particles by ionization," J. Phys. (Moscow) **8**, 201-205 (1944).
- ³¹P. V. Vavilov, "Ionisation losses of high energy heavy particles," Sov. Phys. JETP **5**, 749-751 (1957).

- ³²F. Rohrlich and B. C. Carlson, “Positron-electron differences in energy loss and multiple scattering,” Phys. Rev. **93**, 38-44 (1954).
- ³³T. Tabata, A. Pedro and K. Shinoda, “An analytic formula for the extrapolated range of electrons in condensed materials,” Nucl. Instrum. Methods Phys. Res. B **119**, 463-470 (1996).
645
- ³⁴C. Leroy and P-G. Rancoita, “Chapter 2: Electromagnetic Interaction of Radiation in Matter,” in Radiation Interaction in Matter and Detection (World Scientific Publishing Co. Pte. Ltd, 2004), pp.49.
- ³⁵N. A. Dyson, “Appendix 1: Range-energy relations, etc., for electrons,” in X-rays in atomic and nuclear physics (Longman Group Limited, London, 1973), pp.323.
650
- ³⁶I. Kawrakow, “Accurate condensed history Monte Carlo simulation of electron transport: I. Application to ion chamber response simulations,” Med. Phys. **27** 499-513 (2000)
- ³⁷F. Verhaegen, “Evaluation of the EGSnrc Monte Carlo code for interface dosimetry near high-Z media exposed to kilovolt and ⁶⁰Co photons,” Phys. Med. Biol. **47**, 1691-1705 (2002).
655